Materials Science & Engineering A 946 (2025) 149138

Contents lists available at ScienceDirect

Materials Science & Engineering A

journal homepage: www.elsevier.com/locate/msea

Unlocking strength-ductility synergy in laser additive manufacturing of Ti-Cu alloys via core-shell feedstock design

Dingmeng Xu [a], Wuxin Yang [a,*], Ming Yan [b,**], Malaya Prasad Behera [c], Sarat Singamneni [c], Michael A. Hodgson [a], Yafeng Yang [d], Katsuyoshi Kondoh [e], Peng Cao [a,***]

[a] Department of Chemical and Materials Engineering, The University of Auckland, Private Bag 92019, Auckland, 1142, New Zealand
[b] Department of Materials Science and Engineering, South University of Science and Technology, Shenzhen, 518055, China
[c] Department of Mechanical Engineering, AUT University, New Zealand
[d] State Key Laboratory of Multiphase Complex Systems, Institute of Process Engineering, Chinese Academy of Sciences, Beijing, 100190, China
[e] Joining and Welding Research Institute, Osaka University, Ibaraki, 567-0047, Japan

ARTICLE INFO

Keywords:
Laser powder bed fusion
In situ alloying
Ti-Cu alloy
Core-shell powder
Mechanical properties

ABSTRACT

Solute segregation during conventional manufacturing restricts the development of Ti-Cu alloys despite their potential in biomedical applications. Here, we demonstrate that using core-shell Ti@Cu powders in laser powder bed fusion (PBF-LB/M) enables the fabrication of hypoeutectoid Ti-2.9Cu alloys with >98.4 % density, suppressed segregation, and enhanced chemical homogeneity. The resulting microstructure features equiaxed prior-β grains with ultra-fine α laths and well-distributed nano-sized Ti_2Cu precipitates at lath boundaries, contributing to grain boundary and precipitation strengthening. Compared to blended elemental powders, the core-shell strategy improves ultimate tensile strength by 17 % (from 857 ± 15.9 MPa to 1004.5 ± 18.7 MPa) and ductility by 6.4 % (from 12.6 ± 0.01 % to 13.4 ± 1.0 %). Flow3D simulations indicate enhanced laser–powder energy coupling and a more stable, symmetric melt pool with reduced thermal gradients and uniform convection for the Ti@Cu feedstock, rationalizing the suppressed segregation. This study establishes feedstock architecture as a powerful lever to unlock strength–ductility synergy in laser additively manufactured Ti–Cu alloys for biomedical applications.

The Ti-Cu system holds promise for biomedical and aerospace applications due to its antibacterial properties, high strength, and corrosion resistance [1]. Notably, Ti–6Al–4V–xCu and Ti–Cu alloys show bactericidal activity against E.coli, and S.aureus while maintaining cytocompatibility, underscoring the biomedical relevance of controlled Cu addition [1–3].

However, conventional manufacturing of Ti-Cu alloys is limited by solute segregation during solidification, which produces detrimental heterostructures (e.g., beta-fleck) and has restricted commercial adoption to niche alloys such as Ti-2.5Cu (IMI 230) [4,5]. Laser powder bed fusion (PBF-LB/M), a leading additive manufacturing (AM) technique, provides a different pathway: its rapid solidification (up to 10^8 K/s) promotes non-equilibrium solute trapping, reducing partitioning at the solidification front and thereby suppressing Cu segregation [6,7]. Consistent with this mechanism, recent studies using pre-alloyed Ti-Cu powders achieve fine martensitic microstructures with high strength (~1.1 GPa) [8]. By contrast, in situ alloying from simple elemental powder blends, while cost-effective, suffers chemical inhomogeneity due to the low melting point and high reflectivity of Cu, leading to Cu segregation in localized melt pools and inconsistent properties [9–11]. Consequently, balancing strength and ductility remains difficult; for example, Zhang et al. showed that higher Cu content (8.5 wt%) increases strength but reduces ductility due to the formation of coarse brittle Ti_2Cu particles. Precise control of Cu delivery and compositional homogeneity is crucial in overcoming these issues [12].

Rather than solely optimizing process parameters or applying post-heat treatments to address feedstock-driven inhomogeneity and strength-ductility trade-off, we propose a core-shell feedstock design (Ti@Cu) by coating Cu nanoparticles onto Ti powder via fluidized bed technology (China Patent No. CN109550941B, 2020). Fluidized-bed dry

* Corresponding author.
** Corresponding author.
*** Corresponding author.
E-mail addresses: wyan737@aucklanduni.ac.nz (W. Yang), yanm@sustech.edu.cn (M. Yan), p.cao@auckland.ac.nz (P. Cao).

https://doi.org/10.1016/j.msea.2025.149138
Received 6 August 2025; Received in revised form 12 September 2025; Accepted 15 September 2025
Available online 16 September 2025

coating was prioritized over electroless plating for its solvent-free, large-scale operation and good powder flowability/cleanliness. The wet plating route demanded multi-step chemistry/drying that hinders batch consistency and risk residuals.

Coated powder strategies have been explored for AM in other alloy systems, such as Al-Al_2O_3, Y_2O_3-coated Ni superalloy, and Ti-6Al-4V coated with carbon nanotubes primarily to improve absorptivity, densification, or cracking resistance [13–15]. Our contribution is to translate the core-shell concept to the Ti-Cu system and demonstrate for the first time that a Ti@Cu feedstock for PBF-LB/M can (1) control staged Cu release and melt-pool convection to suppress segregation, (2) yield a more chemically homogeneous microstructure with refined laths, (3) achieve a strength-ductility synergy in the as-built state. To benchmark our method, we conducted PBF-LB/M fabrication of Ti-2.9Cu alloy using conventional mechanically blended Ti/Cu powders as a baseline. Accordingly, 2.9 wt% Cu (hypoeutectoid) leverages antibacterial Cu-ion release while staying well below the eutectoid (~7 wt% Cu) and typical cytotoxicity concerns. This feedstock-process synergy offers valuable insights into advanced powder feedstock modifications and advances in AM of Ti-Cu alloys, providing a scalable solution for producing high-performance applications without post-treatment.

As shown in Fig. 1(a–c), conventional simply blended (SB) Ti-2.9Cu feedstock, prepared by tumble-mixing elemental Ti (14–53 μm) and Cu (15–45 μm) powders, exhibits significant inhomogeneity - a critical challenge in elemental powder blends. EDS mapping reveals an inhomogeneous distribution of Cu powder in the mixed feedstock (Fig. 1c), underscoring the limitations of mechanical mixing for in situ alloying. In contrast, the core-shell (CS) Ti@Cu feedstock (Fig. 1d–f) features a uniform Cu shell (1.5–2 μm thickness) chemically bonded to Ti cores, ensuring homogeneous Cu distribution during printing. This core-shell structure mitigates density-driven segregation and optimizes laser absorptivity, which is critical for stable melt pool dynamics in PBF-LB/M. The CS feedstock shows no gas-induced porosity and a consistent Cu content of 2.93 wt% via ICP-MS (*Inductively coupled plasma mass spectrometry)*, validating its suitability for AM. XRD analysis in Fig. (i) reveals nearly identical diffraction peaks for both powder feedstocks.

The core-shell (CS) structured Ti@Cu powder and simply blended (SB) Ti/Cu elemental powder mixture were subsequently used to fabricate Ti-Cu alloys via PBF-LB/M using a Renishaw AM400 selective laser melting system, with a 1070 nm Nd: YAG laser and a 70 μm focal diameter. The samples are referred to as CS-Ti2.9Cu and SB-Ti2.9Cu, respectively. The dog-bone-shaped specimens (thickness: 3 mm, width: 14 mm, gauge length: 15 mm, and total length: 39 mm) were printed. The laser power was varied between 240W and 320W with a step size of 40W, and scanning speeds varied between 1000 mm/s-1200 mm/s with a step size of 100 mm/s, while hatch spacing and layer thickness were set as 60 μm and 40 μm, respectively. Bulk density was quantified using the Archimedes method. Microstructural characterization was conducted using optical microscopy (OM), SEM-EDS (Hitachi SU-70 field emission), electron backscatter diffraction (EBSD) with an EDAX

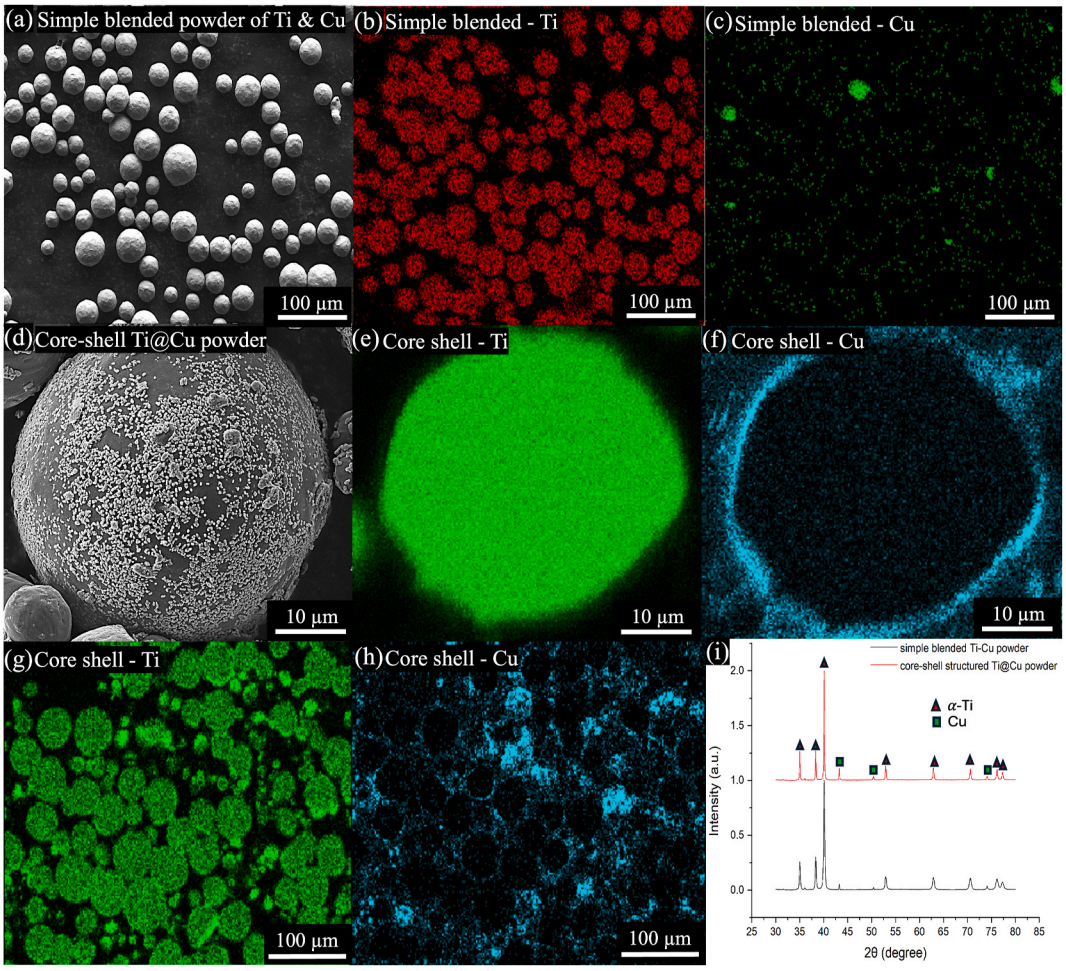

Fig. 1. (a–c) Simple blending of elemental Ti and Cu powder mixture: (a) and (b) are EDS mapping of the distribution of Ti and Cu, respectively. (d–h) Core-shell structured Ti@Cu powder: (d) SEM image of a single Ti@Cu powder, showing the homogeneous distribution of Cu onto the Ti powder; (e–f) EDS mapping of a cross-section of ground Ti@Cu powder; (g–h) EDS mapping of the cross-section of ground Ti@Cu powder at lower magnification. (i) XRD analysis of both powder feedstocks.

Velocity ™ EBSD camera (AMETEK Incorporation, USA), and transmission electron microscopy (TEM, Tecnai F30, USA). The EBSD measurement specimens were prepared by standard mechanical grinding and vibrational polishing procedures (VibroMet®2, Buehler Corporation, USA) at 50 Hz for 4 h. The collected EBSD data were analyzed using OIM Data Analysis software. Transmission electron microscopy (TEM, Tecnai F30, USA) was performed at 300 kV, and the associated selected area electron diffraction (SAED) was used to elucidate the details of the microstructure and the crystal structure of the phase. The samples for the TEM study were prepared using a focused ion beam system (Helios Nanolab 600i, Thermo Fisher Scientific Corporation, USA).

The core-shell approach effectively controls the microstructural outcome in situ, as evidenced by EBSD analysis shown in Fig. 2. The role of Cu in promoting columnar-to-equiaxed transition (CET) and grain refining ability is enhanced, as shown in the inverse pole figure (IPF) and band contrast (BC) map from Fig. 2(a) and (b). The corresponding reconstruction map of parent grains (Fig. 2 a1) shows that fine equiaxed prior grains were achieved. Compared to SB-Ti2.9Cu samples (Fig. 2d and e), the lath is much coarser with more defined grain orientations and columnar prior grains still present. Furthermore, the use of core-shell structure powder feedstock reduces internal residual stresses by preventing the large thermal and compositional gradients, aligning with the evidence from Kernel Average Misorientation (KAM) maps. Fig. 2 (e) reveals a more homogeneous distribution of orientation strain in the CS-Ti2.9Cu alloy compared to SB-Ti2.9Cu (Fig. 2f), which is attributed to a more controlled melting and solidification process during PBF-LB/M. The homogeneously dispersed Cu from the shell minimizes macrosegregation and refines the microstructure by suppressing localized compositional gradients (Fig. 2g). In contrast, the simple blended feedstock exhibits heterogeneous melt pool morphology, resulting in Cu segregation as observed in Fig. 2 (h). Furthermore, CS-Ti2.9Cu yields a clean XRD profile, with significantly sharper and higher-intensity α/α' peaks, indicating greater crystallinity with larger coherent α/α' domains (i.e., reduced peak broadening from microstrain) compared to the simple blend. The Cu-rich intermetallic compounds are undetectable by XRD due to their low volume fraction.

TEM analysis distinctly highlights the critical role of powder feedstock design in governing the microstructural evolution of AM-fabricated Ti–2.9Cu alloys. The core-shell approach, as shown in Fig. 3 (a) and (b), results in a highly homogeneous fine α-Ti lath microstructure, characterized by nano-scaled Ti_2Cu precipitates predominantly confined to lath boundaries, as confirmed in Fig. 3 (e). Such structural uniformity arises from the enhanced local Cu distribution during melting and rapid solidification, effectively suppressing large-scale segregation and subsequent eutectoid decomposition.

In contrast, SB-Ti2.9Cu alloy results in a heterogeneous microstructure (Fig. 3f–h), featuring a coarser α-Ti lath matrix with a higher density of Ti_2Cu nanoparticles and localized areas of eutectoid lamellar structure, along with the presence of brittle $TiCu_3$ at lamellar interfaces (Fig. 3 g1-g3). A plausible mechanism is that uneven powder

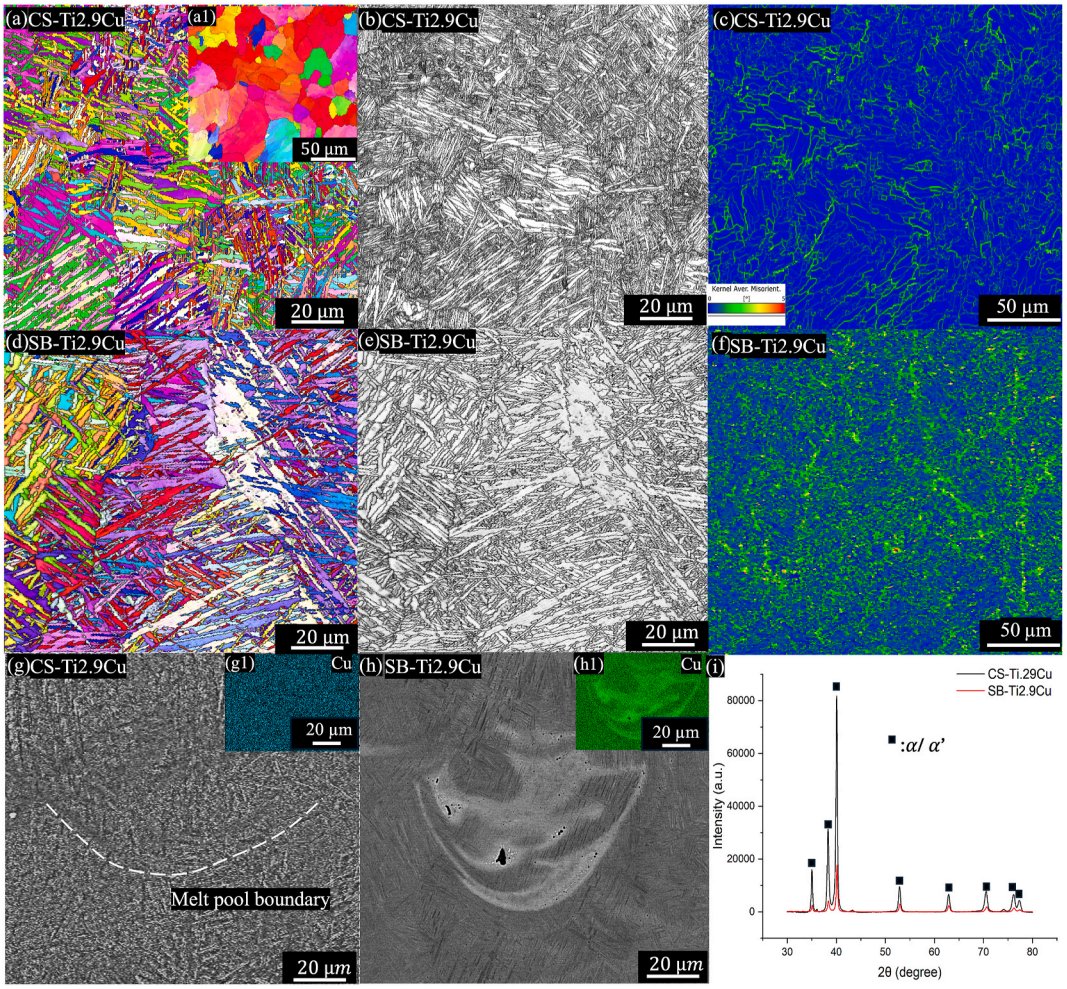

Fig. 2. EBSD of CS-Ti2.9Cu: (a) IPF map with fine α-laths; (a1) reconstructed equiaxed prior-β grains; (b) band contrast map; (c) KAM map. EBSD of SB-Ti2.9Cu: (d) IPF map with coarser α-laths; (e) band contrast; (f) KAM map. (g) SEM image of CS-Ti2.9Cu revealing no apparent Cu segregation with (g1) EDS mapping of Cu element; (h) SEM image of SB-Ti2.9Cu revealing Cu segregation with (h1) EDS mapping of Cu element; (i) XRD patterns of both as-built samples.

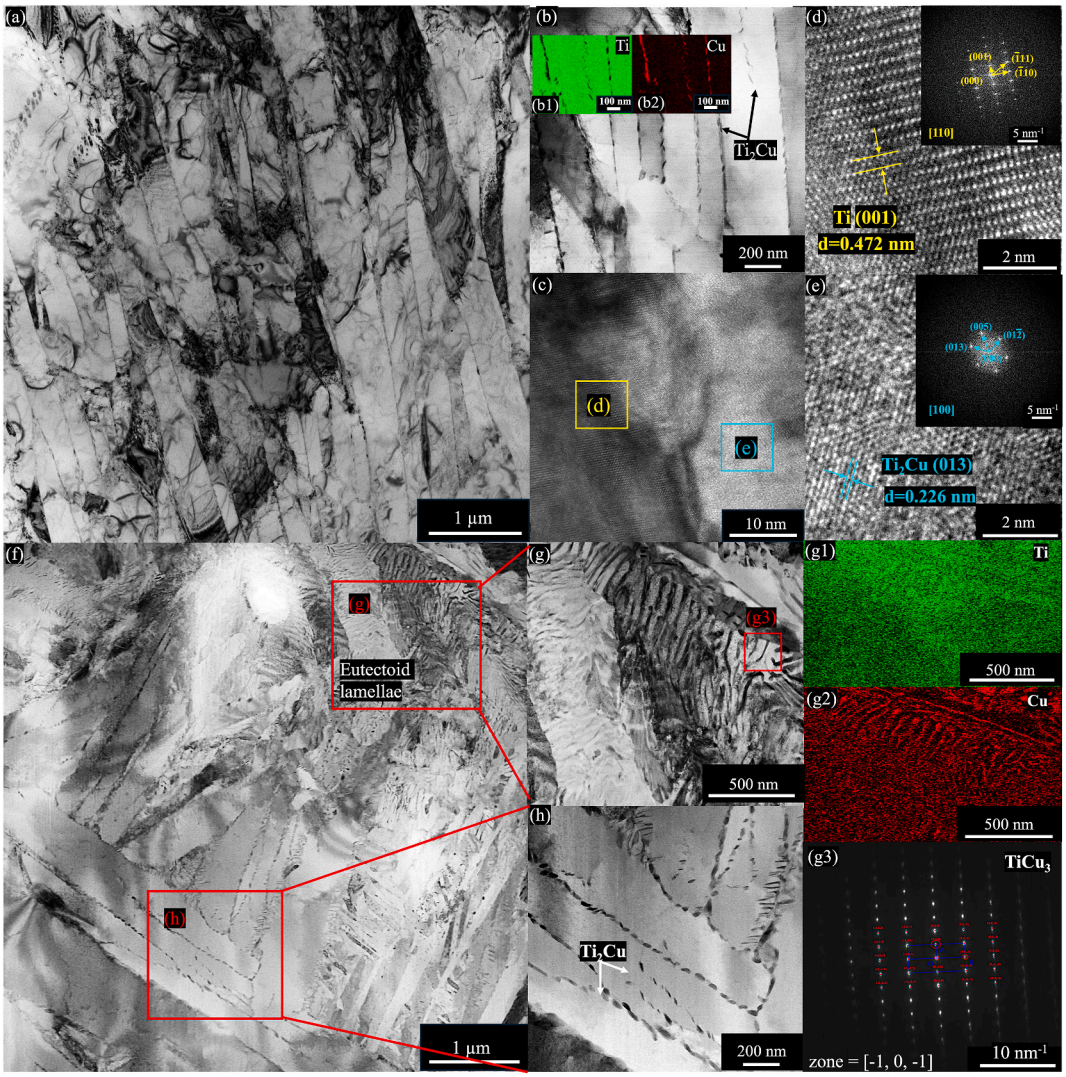

Fig. 3. TEM of CS-2.9Cu: (a) and (b) are STEM-HAADF BF images showing the as-built microstructure with (b1) and (b2) showing the X-ray maps of Ti and Cu taken from (b); (c) High-resolution TEM (HRTEM) image at the lath boundary area. (d) The corresponding Fast Fourier Transform (FFT) image of area 'd' highlighted in yellow from (c), confirming the α lath; (e) The corresponding FFT image of area 'e' highlighted in blue from (c), confirming Ti_2Cu distributed at the boundary. TEM of SB-Ti2.9Cu: (f) STEM-HAADF BF image shows the heterogeneous structure; (g) The localized area of eutectoid lamellar structure from (f). (h) Fine α-Ti lath matrix with Ti_2Cu precipitate; (g1) and (g2) are the X-ray maps of Ti and Cu taken from the area highlighted in red from (g); (g3) The corresponding SAED pattern of the region highlighted in red from (g), confirming the presence of $TiCu_3$ at the boundary of eutectoid lamellar. (For interpretation of the references to colour in this figure legend, the reader is referred to the Web version of this article.)

distribution and local differences in energy absorption, creating pronounced local Cu-rich pockets and slower solidification dynamics, thus favoring eutectoid reactions which are rationalized via simulation. Ti_2Cu formation with limited back-diffusion creates Ti-rich seams at colony interfaces, favoring interfacial $TiCu_3$. Consequently, the refined Ti_2Cu network formed through the CS strategy offers robust grain boundary pinning and dislocation impediment without sacrificing ductility. Whilst the eutectoid lamellae and $TiCu_3$ precipitate prevalent in SB introduce brittle interfaces, diminishing overall mechanical performance. These observations underscore the advantage of core-shell powder design in achieving superior strength-ductility synergy via precise microstructural control.

To further explain the origin of the refined and homogeneous microstructures observed in the CS-Ti2.9Cu alloy, the laser-powder melt-pool fields via Flow-3D simulations were analyzed. Fig. 4 reveals distinct differences in melt pool dynamics, thermal gradients, and compositional uniformity between simple-blend (SB) and core-shell (CS) powder configurations during PBF-LB/M. In the SB case (Fig. 4a and b), the melting point disparity between Ti and Cu causes Cu to melt prematurely, generating localized Cu-rich melt zones. These regions produce steep thermal gradients and turbulent melt flow that promote pronounced solute segregation and compositional heterogeneity. The resulting melt pool is unstable and prone to localized phase separation upon solidification, consistent with the heterogeneous microstructure observed in Fig. 3f–h.

In contrast, the CS design yields near-synchronous shell/core melting and particle-scale Cu delivery, producing a uniform thermal profile and smooth, symmetric melt flow (Fig. 4d and e). The Cu is inherently dispersed at the particle scale, ensuring a homogeneous composition throughout the melt pool and preventing sharp temperature spikes. Consequently, the CS melt pool attains a slightly larger molten volume and deeper penetration into the substrate, with the high-temperature region more evenly distributed along the track. The temperature contours in Fig. 4 (f) show a smoother, bowl-shaped profile, as opposed to the sharper, more protruding hot spot in the blended case (Fig. 4c). It also exhibits stable convection that uniformly mixes the molten Ti and Cu. These favourable melt pool characteristics mitigate thermal gradients and solute segregation, explaining the refined, homogeneous

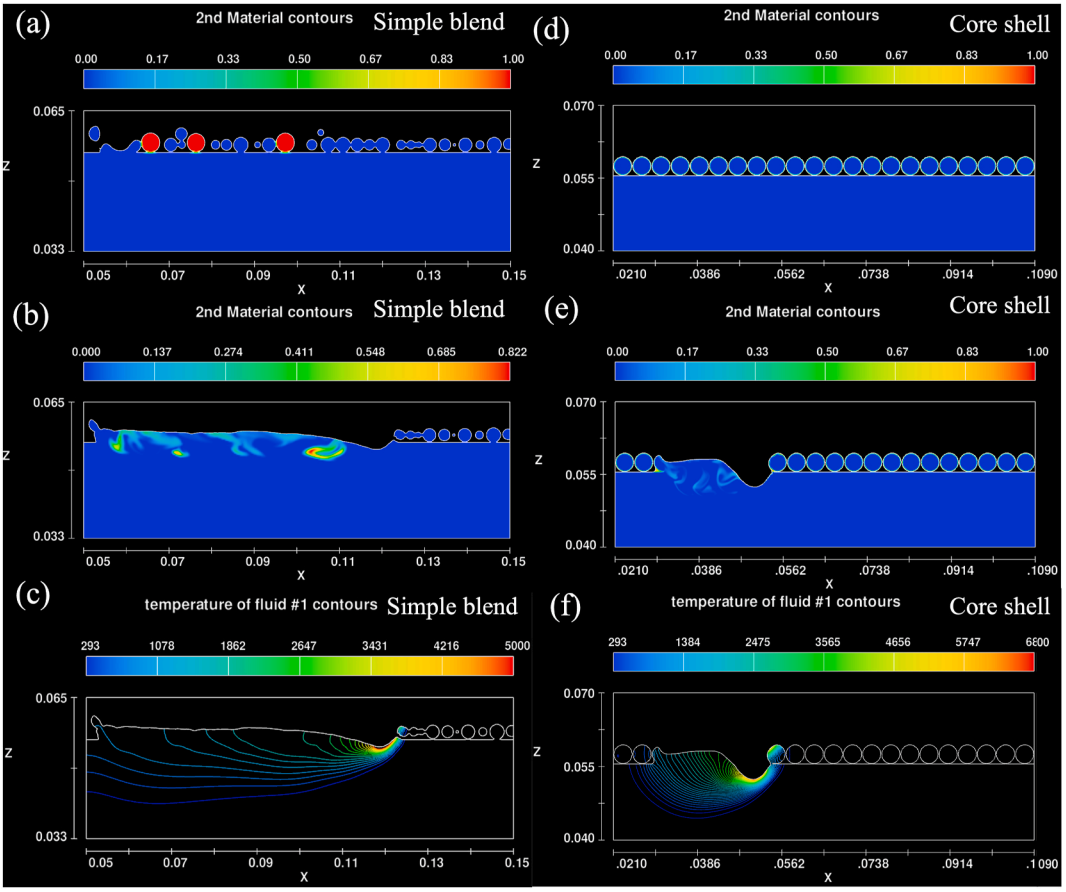

Fig. 4. Flow 3D simulation of PBF-LB/M processes: (a,d) Initial material distribution of simple blended and core-shell powders; (b,e) Material contours during melting and diffusion; (c, f) Temperature fields during progressive melting for blended and core-shell powders, respectively.

microstructure observed in the CS-Ti2.9Cu alloy (Fig. 3(a) and (b)).

As shown in Fig. 5a, the CS powder design enhances the ultimate tensile strength of Ti–2.9Cu by approximately 17 %, increasing from 857 ± 15.9 MPa in the blended condition to 1004.5 ± 18.7 MPa, and increasing ductility by 6.4 %, from 12.6 ± 0.01 % to 13.4 ± 1 %. The strength-ductility map of additively manufactured Ti-based alloys (Fig. 5b) further demonstrates that the CS-Ti2.9Cu alloy effectively surpasses the conventional strength-ductility trade-off and approaches the performance of workhorse Ti-6Al-4V, despite being a binary, in-situ alloyed system. Corresponding fracture surface analyses reveal that both the CS and SB Ti-2.9Cu alloys exhibit mixed fracture features comprising ductile dimples and brittle facets (Fig. 5c and d); the CS alloy displays a more ductile fracture mode, as evidenced by its finer and more uniformly distributed dimples, consistent with its slightly enhanced elongation and nano-Ti_2Cu/α-lath architecture derived from stabilized melt-pool fields.

In the simple blending (SB) case, hard and brittle interfacial $TiCu_3$ decorates lamellar boundaries, disrupting load transfer and promoting early microcracks, which limit uniform elongation. Flow-3D indicates that SB develops Cu-rich melt pockets, steeper thermal gradients, and vortical recirculation (Fig. 4), fostering eutectoid α+Ti_2Cu lamellae and $TiCu_3$ at interfaces. In contrast, at 2.9 wt% Cu, the CS architecture delivers Cu at the particle scale and stabilizes the melt pool, lowering composition fluctuations and the lamellar area fraction. This promotes dual-phase boundary shells (Ti_2Cu/α) that help stabilize equiaxed prior-β grains and retain nano-Ti_2Cu on α-lath boundaries for grain-boundary strengthening without embrittlement, explaining the combined strength and ductility gains. Quantitatively, the strength–ductility index ($\sigma_{(UTS)} \times \varepsilon_f$) increases from ~108 to ~135 MPa-% (~25 % increase) [16,17], reflecting higher tensile energy-absorption capacity. This is practically valuable for load-bearing biomedical components where notch sensitivity and early crack initiation dominate failure, and where the higher strength permits thinner sections without sacrificing ductility.

In conclusion, using core-shell Ti@Cu powders for PBF-LB/M in-situ alloying markedly improves the chemical and microstructural homogeneity of Ti–2.9Cu builds. The core-shell powder feedstock leads to a more uniform and desirable solidification pathway that suppresses the heterogeneous structure of coarse eutectoid formation, resulting in a fine and consistent microstructure of α lath with dispersed nano-sized Ti_2Cu throughout the material. Such a microstructure directly contributes to the enhanced mechanical performance, achieving ~17 % UTS gain with a good ductility increase over the blended powder case that suffers from brittleness due to segregated Cu at lamellae boundaries. Fundamentally, the core-shell powder strategy demonstrates that feedstock-controlled stabilization of the melt pool promotes uniform solute trapping, which in turn yields tailored transformation products and a superior strength–ductility balance in the as-built condition. Future work will be focused on precipitation control rather than homogenization via heat treatment to tailor phase evolution and intermetallic distribution, with the aim of further optimizing the strength-ductility response of the Ti-Cu alloy. In parallel, we will explore higher Cu and multi-element or multilayer shells/cores for graded chemistries and additional functionality via single-powder in-situ alloying.

CRediT authorship contribution statement

Dingmeng Xu: Writing – original draft, Methodology, Investigation, Formal analysis. **Wuxin Yang:** Writing – review & editing, Investigation, Formal analysis. **Ming Yan:** Writing – review & editing, Resources,

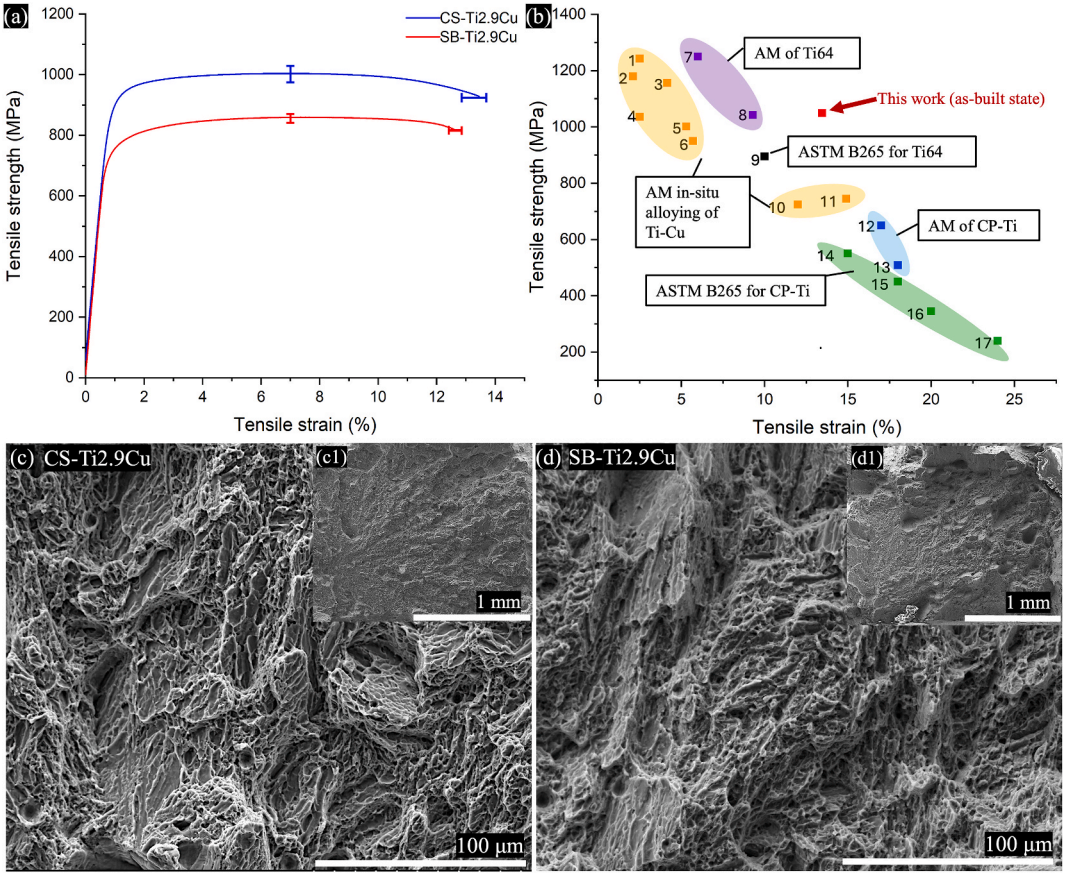

Fig. 5. (a) Tensile properties of CS-Ti2.9Cu and SB-Ti2.9Cu alloys. (b) Strength–ductility map of additively manufactured Ti-based alloys for comparison: 1. [18], 2 [12]. 3. [19], 4. [20], 5. [20], 6. [12], 7. [21], 8. [22], 9.ASTM B265-15 Grade 5 Ti-6Al-4V Grade 5, 10. [20], 11. [12], 12. [23], 13. [24], 14. ASTM B265-15 Grade 4 CP-Ti, 15. ASTM B265-15 Grade 3 CP-Ti, 16. ASTM B265-15 Grade 2 CP-Ti, 17. ASTM B265-15 Grade 1 CP-Ti. (c) Fractography of the CS-Ti2.9Cu alloy, with an enlarged view in (c1). (d) Fractography of Ti2.9Cu alloy, with an enlarged view in (d1).

Investigation. **Malaya Prasad Behera:** Investigation. **Sarat Singamneni:** Resources, Methodology, Investigation. **Michael A. Hodgson:** Writing – review & editing, Formal analysis. **Yafeng Yang:** Resources, Formal analysis. **Katsuyoshi Kondoh:** Formal analysis. **Peng Cao:** Writing – review & editing, Supervision, Funding acquisition, Conceptualization.

Declaration of competing interest

The authors declare that they have no known competing financial interests or personal relationships that could have appeared to influence the work reported in this paper.

Acknowledgments

The Royal SocietyTe Apārangi funded this work through its Marsden Fund (Grant no. UOA2114).

Data availability

Data will be made available on request.

References

[1] E. Zhang, F. Li, H. Wang, J. Liu, C. Wang, M. Li, K. Yang, A new antibacterial titanium–copper sintered alloy: preparation and antibacterial property, Mater. Sci. Eng. C 33 (7) (2013) 4280–4287.
[2] J. Liu, F. Li, C. Liu, H. Wang, B. Ren, K. Yang, E. Zhang, Effect of Cu content on the antibacterial activity of titanium–copper sintered alloys, Mater. Sci. Eng. C 35 (2014) 392–400.
[3] Z. Ma, L. Ren, R. Liu, K. Yang, Y. Zhang, Z. Liao, W. Liu, M. Qi, R.D.K. Misra, Effect of heat treatment on Cu distribution, antibacterial performance and cytotoxicity of Ti–6Al–4V–5Cu alloy, J. Mater. Sci. Technol. 31 (7) (2015) 723–732.
[4] M.A. Hayat, S.M.A. Sulimam, An economical heat treatment cycle for IMI Ti-230, Mater. Manuf. Process. 13 (2) (1998) 203–212.
[5] A. Kawakami, Study on Segregation Behavior of Alloying Elements in Titanium Alloys During Solidification, 2002.
[6] M. Chen, Y. Ning, X. Sun, T. Liu, H. Wei, K. Zhang, W. Zhou, Z. Zhu, W. Zhai, W. Liao, Manipulating microstructure and mechanical property during laser powder bed fusion: multi-material, in-situ alloying, and processing, J. Alloys Compd. 1007 (2024) 176438.
[7] D. Xu, W. Yang, P. Cao, In situ multi-metal alloying in laser-based additive manufacturing: a concise review, Compos. B Eng. 299 (2025) 112443.
[8] H. Liu, H. Wang, L. Ren, D. Qiu, K. Yang, Antibacterial copper-bearing titanium alloy prepared by laser powder bed fusion for superior mechanical performance, J. Mater. Sci. Technol. 132 (2023) 100–109.
[9] M.H. Mosallanejad, B. Niroumand, A. Aversa, D. Manfredi, A. Saboori, Laser powder bed fusion in-situ alloying of Ti-5%Cu alloy: process-structure relationships, J. Alloys Compd. 857 (2021) 157558.
[10] A.M. Vilardell, I. Yadroitsev, I. Yadroitsava, M. Albu, N. Takata, M. Kobashi, P. Krakhmalev, D. Kouprianoff, G. Kothleitner, A.d. Plessis, Manufacturing and characterization of in-situ alloyed Ti6Al4V(ELI)-3 at.% Cu by laser powder bed fusion, Addit. Manuf. 36 (2020) 101436.
[11] D. Xu, W. Yang, M.P. Behera, S. Singamneni, M.A. Hodgson, P. Cao, Creating heterostructures via laser powder bed fusion using titanium and stainless steel mixtures, Mater. Sci. Eng., A 915 (2024) 147260.
[12] D. Zhang, D. Qiu, M. Gibson, Y. Zheng, H. Fraser, D. StJohn, M. Easton, Additive manufacturing of ultrafine-grained high-strength titanium alloys, Nature 576 (2019) 91–95.
[13] L. Wang, M. Li, X. Lin, T. Gui, H. Chai, W. Huang, The distribution of Y2O3 during selective laser melting of IN625/Y2O3 core-shell powders, Adv. Powder Technol. 35 (9) (2024) 104609.
[14] I.A. Pelevin, A.Y. Nalivaiko, D.Y. Ozherelkov, A.S. Shinkaryov, S.V. Chernyshikhin, A.N. Arnautov, S.V. Zmanovsky, A.A. Gromov, Selective laser melting of Al-Based matrix composites with Al(2)O(3) reinforcement: features and advantages, Materials 14 (10) (2021).

[15] Y. Liu, S. Li, R.D.K. Misra, K. Geng, Y. Yang, Planting carbon nanotubes within Ti-6Al-4V to make high-quality composite powders for 3D printing high-performance Ti-6Al-4V matrix composites, Scr. Mater. 183 (2020) 6–11.
[16] Y. Wang, C. Huang, X. Ma, J. Zhao, F. Guo, X. Fang, Y. Zhu, Y. Wei, The optimum grain size for strength-ductility combination in metals, Int. J. Plast. 164 (2023) 103574.
[17] C. Zhang, X. Bao, M. Hao, W. Chen, D. Zhang, D. Wang, J. Zhang, G. Liu, J. Sun, Hierarchical nano-martensite-engineered a low-cost ultra-strong and ductile titanium alloy, Nat. Commun. 13 (1) (2022) 5966.
[18] Y. Ren, X. Liu, H. Wang, Y. Yang, I. Baker, P. Wang, H. Wu, Unraveling the inherent anisotropic properties of in situ alloyed copper-modified titanium alloys produced by laser powder bed fusion, J. Alloys Compd. 966 (2023) 171323.
[19] J. Wang, K. Liu, X. Xue, J. Li, B. Chen, Columnar-to-equiaxed transition mechanism and remarkable strengthening effect in additive manufactured pure titanium induced by copper addition, Mater. Char. 209 (2024) 113750.
[20] Q. Wang, K. Zhang, W. Niu, Microstructural characteristic and mechanical properties of titanium-copper alloys in-situ fabricated by selective laser melting, J. Alloys Compd. 885 (2021) 161032.
[21] B. Vandenbroucke, J.P. Kruth, Selective laser melting of biocompatible metals for rapid manufacturing of medical parts, Rapid Prototyp. J. 13 (4) (2007) 196–203.
[22] A. Nourollahi, R. Razavi, M. Barekat, M. Anaraki, M. Erfanmanesh, Microstructural investigation of direct laser deposition of the Ti-6Al-4V alloy by different melt pool protection conditions, J. Mater. Res. Technol. 13 (2021).
[23] B. Wysocki, P. Maj, A. Krawczyńska, K. Rożniatowski, J. Zdunek, K. J. Kurzydłowski, W. Święszkowski, Microstructure and mechanical properties investigation of CP titanium processed by selective laser melting (SLM), J. Mater. Process. Technol. 241 (2017) 13–23.
[24] N. Singh, P. Hameed, R. Ummethala, G. Manivasagam, K.G. Prashanth, J. Eckert, Selective laser manufacturing of Ti-based alloys and composites: impact of process parameters, application trends, and future prospects, Mater. Today Adv. 8 (2020) 100097.